Spatial Location Engineering of Oxygen Vacancies for Optimized Photocatalytic H_2 Evolution Activity

Wentuan Bi, Chunmiao Ye, Chong Xiao, Wei Tong, Xiaodong Zhang, Wei Shao, and Yi Xie**

Environmental crisis, coupled with the increasing global energy consumption have triggered keen interests in renewable energy. The efficient conversion of solar energy into chemical fuels is expected to be an ideal green technology. Of these, the photo-driven water splitting reaction which directly converts solar energy into chemical energy is a highly appreciated alternative.[1–3] Since the discovery of water photooxidation on a TiO_2 photoanode in 1972, impressive progress has been made in exploiting cheap, efficient, and stable photocatalysts.[4–8] However, the relatively low energy conversion efficiency is still one of the most important factors restricting the practical application of this technology. To overcome this bottleneck, in-depth and full comprehensive understanding of the physical and chemical processes during this reaction is urgently needed.

As is known, photocatalytic reactions take place at the surface of photocatalysts.[9] Therefore, the improvement of surface area is generally considered to potentially realize the high photocatalytic efficiency. Up till now, extensive efforts have been devoted to maximize the surface area of the catalysts via designing various nanostructures.[10–12] However, increasing the catalyst surface area does not always bring the desired performance improvement. For instance, as reported by Osterloh, the catalytic activity of the $K_4Nb_6O_{17}$ nanosheets (KNbO NSs) with a thickness of 2 nm is only comparable to their bulk counterparts.[13] So what are the key factors affecting the catalytic process? Our recent study on ultrathin BiOCl nanosheets demonstrates that the predominant defects change as the thickness reduces to the atomic scale, which experimentally leads to the significantly improved photocatalytic performance.[14] Inspired by this result, it is reasonable to believe that the defects and the associated electronic structure changes should play the decisive role in determining the photocatalytic efficiency. Although the KNbO NSs with thickness down to few nanometers can be obtained from the exfoliation process, the detailed analysis of niobates structures reveals that either Nb atoms or O atoms are difficult to escape from the lattice due to the strongly bonded Nb-O bonds within the layer,[15] eventually leading to the previously reported comparable catalytic performance between the KNbO NSs and their bulk counterparts. From this perspective, introducing defects artificially should be highly desirable for promoting the solar-driven photocatalytic activity of niobates.

Oxygen vacancies, the most common defects in oxide semiconductors, provide new insights to control the charge separation process, as well as engineer the electronic structure of semiconductors.[16–19] Meanwhile, they can be easily introduced via thermal treatment in a reductive atmosphere. Unfortunately, an ongoing debate over the role of oxygen vacancies in the photocatalytic process has hindered further progress in realizing higher energy conversion efficiency.[20,21] The cause of this controversy is probably the neglect of the influence of oxygen vacancies in different spatial location.[22] Taking this fact into consideration, the ability to manipulate the spatial location of oxygen vacancies at the atomic level becomes the key prerequisite for solving this problem. The recent high-profile atomically thick nanosheets provide an ideal platform to realize high reaction area, as well as overcome the charge carrier diffusion restrictions.[11] By virtue of these structural advantages, oxygen vacancies in ultrathin nanosheets can be expected to be directly involved in the catalytic reaction. Consequently, the design of atomic-thickness nanosheets containing oxygen vacancies seems to be a suitable strategy to provide clear-cut evidences for elucidating the role of surface oxygen vacancies on the photocatalytic performance.

Herein, we highlight the spatial location engineering of defects to successfully optimize the photocatalytic activity of $K_4Nb_6O_{17}$. The oxygen vacancies are introduced through controllable reduction in a reductive atmosphere (the synthesis process and characterizations are shown in detail in the experimental section). It should be noted that this feasible strategy produces defective KNbO NSs with no organic species absorbing on the surface compared to the conventional intercalation-exfoliation process, thus exclude the impact

W. T. Bi, C. M. Ye, Dr. C. Xiao, Dr. X. D. Zhang, W. Shao, Prof. Y. Xie
Hefei National Laboratory for Physical Sciences at the Microscale, and Collaborative Innovation Center of Chemistry for Energy Materials
University of Science & Technology of China
Hefei, Anhui 230026, China
E-mail: cxiao@ustc.edu.cn; yxie@ustc.edu.cn
Prof. W. Tong
High Magnetic Field Laboratory
Chinese Academy of Sciences
Hefei, Anhui 230031, China

DOI: 10.1002/smll.201303548

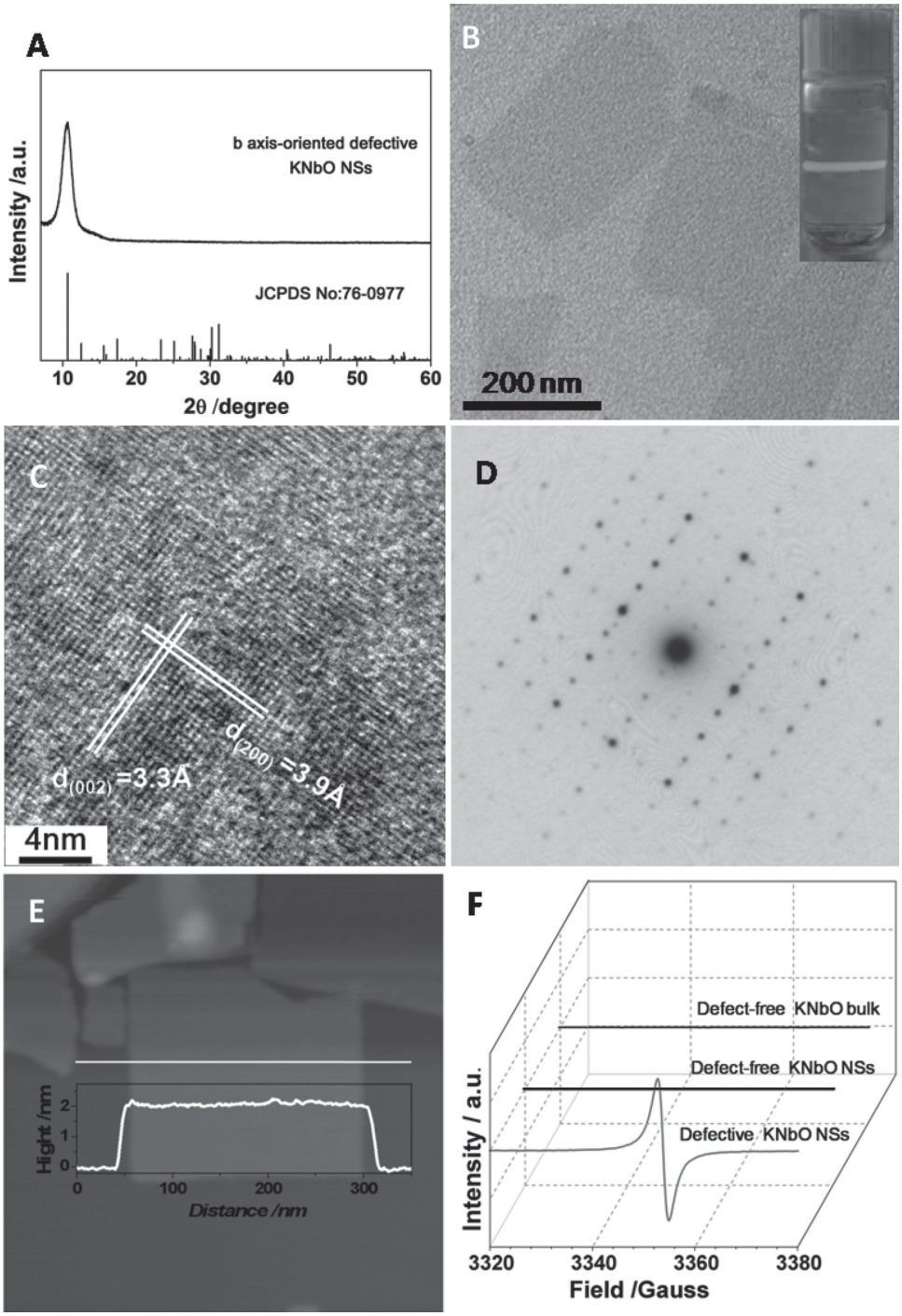

Figure 1. Characterization of the defective $K_4Nb_6O_{17}$ ultrathin nanosheets. A) XRD pattern of the assembled film, showing the *b*-axis orientation of the ultrathin nanosheets. B) TEM image and the homogeneously dispersed suspension displaying the Tyndall effect (inset). C) HRTEM image and D) the corresponding selected-area electron diffraction. E) AFM image and the corresponding height profile. F) ESR spectra of the defective, defect-free $K_4Nb_6O_{17}$ nanosheets and bulk, respectively.

of surface contamination, providing a reliable platform to investigate the relationship between material structure features and the performance of photocatalysts. The structural information of the sample is revealed by X-ray diffraction pattern (XRD), high-resolution transmission electron microscopy (HRTEM) and selected-area electron diffraction (SAED). The XRD pattern provides direct phase information for the defective nanosheets. As shown in **Figure 1**A, the sole strong diffraction peak of the vacuum-filtration treated defective KNbO NSs film confirms the $K_4Nb_6O_{17}$ structure and the highly *b*-axis orientation. Figure 1B is the transmission electron microscopy (TEM) image, showing freestanding nanosheets with lateral dimensions varied from 100 to 200 nm. The inset of Figure 1B shows a well defined Tyndall light scattering observed in the transparent colloidal suspension of the defective KNbO NSs. It is worthy to mention

that the suspension is very stable and no aggregation can be observed after standing for months. To further probe the micro-structural characteristics, HRTEM image is shown in Figure 1C. As seen from the well-resolved lattice features, the nanosheets are highly crystallized, and the interplanar distances coincide well with that of (200) and (002) facets, respectively. The HRTEM and the corresponding SAED pattern in Figure 1D further confirm that the as-synthesized defective KNbO NSs are *b* axis-oriented. Atomic force microscopy (AFM) provides clear-cut evidence to identify the thickness of the nanosheets. As depicted in Figure 1E, the AFM image and the corresponding height profile clearly show the typical samples with the smooth and large sheet-like morphology and a height down to about 2 nm, which is approximately equal to half of the unit cell parameter along the [010] direction. All above results clearly demonstrate that defective KNbO NSs with high crystallinity and orientation along *the b axis* have been obtained. The electron spin resonance (ESR) measurement provides fingerprint evidences for probing oxygen vacancies. As shown in the Figure 1F, a sharp signal at $g = 2.004$, which is identified as the electrons trapped on oxygen vacancies,[23] is detected only in the defective KNbO NSs, verifying the successful introduction of oxygen vacancies. Moreover, the absence of the signal in the defect-free KNbO NSs again confirms that reducing the thickness alone cannot introduce oxygen vacancies. The X-ray photoelectron spectroscopy (XPS) measurements provide auxiliary evidence of the presence of oxygen vacancies, in that the existence of oxygen vacancies leads to distinct coordinations of oxygen species. As shown in the O 1s XPS in Figure S3, a new peak located at 531.5 eV is observed in the defective KNbO NSs, which can be assigned to oxygen vacancies.[24] Combining with the ESR and XPS characterizations above, we can conclude that oxygen vacancies are successfully introduced to the defective KNbO NSs, providing the prerequisite for investigating the role of surface oxygen vacancies.

To evaluate the light-driven hydrogen generation activity of the defective KNbO NSs, the rate of hydrogen evolution is examined in 20 vol% methanol aqueous solution under the illumination of a 300 W Xe lamp. As depicted in **Figure 2**A, the defective KNbO NSs show a remarkable hydrogen evolution rate of 1616 $\mu mol \cdot g^{-1} \cdot h^{-1}$. As far as we know, the hydrogen evolution rate is much higher than most $K_4Nb_6O_{17}$ nanostructures without loading noble metal particles reported previously.[13] The stability of the defective KNbO NSs is also investigated by recording its time dependent H_2 evolution yield. As shown in Figure 2B, the H_2 produced is evacuated every 4 h in successive runs. Obviously, hydrogen production shows an approximately linear relation with illumination time in the entire measurement process, suggesting the persistent gas production. Meanwhile, negligible decrease in hydrogen production is observed after eight cycles. These results indicate excellent stability of the present material for photocatalytic H_2 evolution.

For a long time, it has been an extremely controversial issue on the role of oxygen vacancies in the catalytic reaction. Are the oxygen vacancies in the ultrathin nanosheets indeed attributed to the enhanced H_2 evolution efficiency? To solve this confusion, defect-free KNbO NSs, the defect-free KNbO bulk and the defective KNbO bulk with oxygen vacancies are also synthesized under the similar synthesis conditions for a comparison (the characterizations are shown in detail in the supporting materials Figure S1–S2). As the experiments illuminate, the defective KNbO NSs achieve approximately 6-fold increase in the hydrogen evolution rate compared with the defect-free KNbO NSs, while the defective KNbO bulk possesses 3-fold hydrogen evolution rate in comparison with the defect-free KNbO bulk. In addition, as shown in Figure S4 the photocatalytic hydrogen evolution rate of the annealed defective KNbO NSs, which is free of oxygen vacancies, is obviously decreased, unambiguously revealing that the introduction of oxygen vacancies is an efficient strategy to promote H_2 evolution.

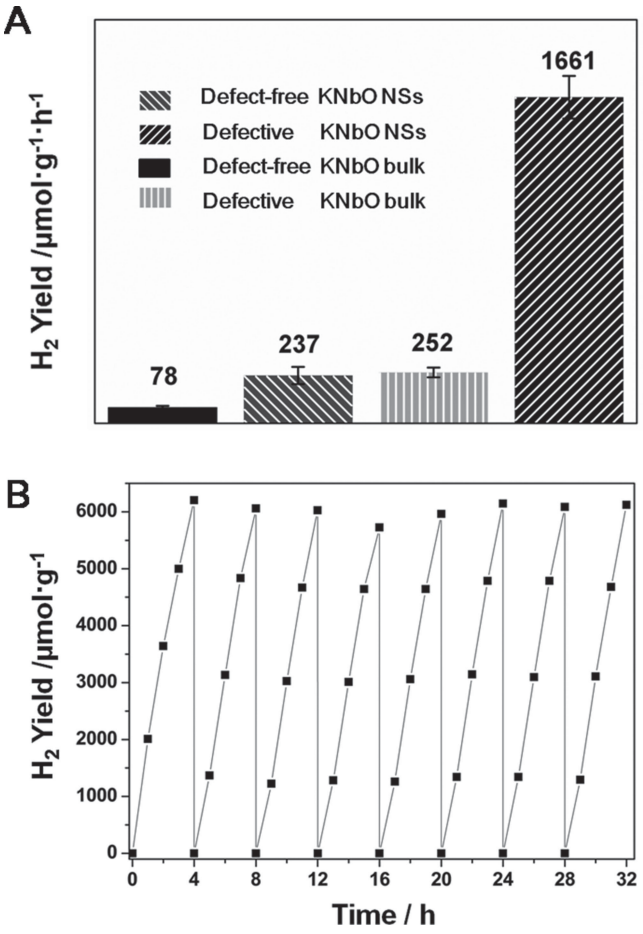

Figure 2. A) A comparison of H_2 evolution activity between the defective $K_4Nb_6O_{17}$ nanosheets, the defect-free $K_4Nb_6O_{17}$ nanosheets, the defect-free $K_4Nb_6O_{17}$ bulk and the defective $K_4Nb_6O_{17}$ bulk. B) A typical time course of H_2 evolution of the defective $K_4Nb_6O_{17}$ nanosheets. Reaction condition: 10 mg catalyst, 200 mL 20 vol% aqueous methanol, under a 300 W Xe lamp.

In order to shed light on the role of oxygen vacancies in different spatial location, detailed comparison of the H_2 evolution activity is conducted between the defective nanosheets and defective bulk with an equivalent oxygen vacancy concentration, which is confirmed by ESR measurement in Figure S5. As shown in Figure 2A, the defective KNbO NSs possess 6 times the hydrogen evolution rate in comparison with the defective KNbO bulk. The surface area

NANO MICRO small

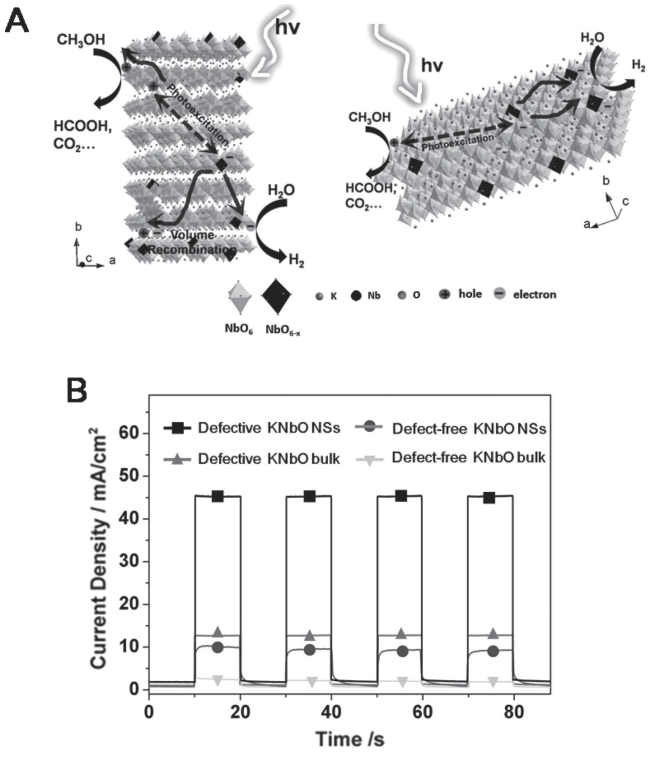

Figure 3. A) Schematic illustration of the photo-generated carriers migration paths in the defective $K_4Nb_6O_{17}$ bulk and nanosheets. B) A comparison of photocurrent density measured at 0.6 V bias voltage versus Ag/AgCl in 0.5 M Na_2SO_4 aqueous solution under illumination of a 300 W Xe lamp.

is well known to closely relate to the catalytic performance. However, in our case, the hydrogen evolution rate of defect-free KNbO NSs is about 3 times that of the defect-free KNbO bulk. Therefore, we can conclude that the distinction in hydrogen evolution rate is mainly sourced from the different spatial location of oxygen vacancies. It is well known that the charge separation and migration should significantly affect the photocatalytic performance, which can be verified in the photocurrent response experiment. As shown in **Figure 3**B, the defective KNbO NSs show the largest photocurrent density, which confirms the intrinsic advantages of this structure in facilitating the separation of the photo-generated carriers. The photo-generated carriers migration paths in the defective KNbO bulk and NSs are schematically illustrated in Figure 3A. The defective KNbO NSs, which are rich in surface oxygen vacancies, provide more surface electrons trapping sites, thus significantly facilitate the separation of the photo-generated carriers. In addition, it has been theoretically verified that the chemical absorption of water molecules is energetically favorable on the defective surface in some other compounds.[25,26] Similarly, in our case, photo-generated electrons can react with the water molecules trapped by surface oxygen vacancies as soon as it is generated. Compared with the corresponding defective KNbO bulk, the reduced charge migration paths and the fast charge separation in the defective ultrathin nanosheets effectively reduce the probability of hole-electron recombination, providing more charge carriers for the overall H_2 evolution reaction.

Furthermore, the surface-localized oxygen vacancies can strongly influence the electronic structure, which should be responsible for the significantly improved photocatalytic performance. As shown in the digital pictures in **Figure 4**A, the atomic-thin defective KNbO NSs exhibit a pale gray color, which guarantees a broadened light absorption range. UV–Vis spectra in Figure 4A confirm that the reduced samples demonstrate enhanced optical absorption in the visible region compared with their defect-free counterparts. Meanwhile, a substantial red-shift in the absorption edges is observed in the reduced samples, indicating a decreasing band gap. In addition to the optical absorption, the carrier transport property is critical for making a high performance photocatalyst. To gain insight into the carrier transport property of the defective KNbO NSs, Mott–Schottky plots are performed to determine the carrier densities and the flat band potentials. As shown in Figure 4B, the defective KNbO NSs possess a relatively smaller slope, indicating a higher carrier density, which will certainly facilitate the charge transport during the photocatalytic H_2 evolution process. The flat band potential of the defective KNbO NSs shows a positive shift of 0.2eV, which could be ascribed to the oxygen vacancies induced band gap narrowing. A comparison of energy diagrams for the defect-free KNbO NSs and defective KNbO NSs is schematically illustrated based on the XPS valence band spectra (Figure 4C) and the band gaps calculated from the UV-Vis spectra. As shown in Figure 4D, the positive shift of the conduction band is consistent well with that estimated from the Mott–Schottky plots. Combining with the UV–Vis spectra, Mott–Schottky plots and the XPS valence band spectra above, we can conclude that surface oxygen vacancies can effectively narrow down the band gap and improve the optical absorption of the KNbO NSs. This conclusion is also confirmed by the fact that when the defective KNbO NSs are annealed in air to eliminate the oxygen vacancies, as is shown in Figure 4A, the sample turns white.

In summary, our developed novel pathway based on the spatial location engineering of defects not only can be successfully applied to optimize the phototcatalytic performance, but also provide some new insights for the in-depth understanding of oxygen vacancies effect on the photocatalytic property, thereby opening up a feasible and effective approach for engineering the defects of semiconductors to achieve high-efficient hydrogen evolution photocatalysts. The insights gained from the experimental results in this study indicate that the surface oxygen vacancies not only narrow the band gap and enhance the optical absorption, which promote the generation of electron and hole, but also reduce the migration paths, which effectively separates the photo-induced electron-hole pairs. As a result, taking $K_4Nb_6O_{17}$ as an example, the defective $K_4Nb_6O_{17}$ ultrathin nanosheets show the significantly accelerated H_2 evolution rate, which is extraordinarily enhanced by 20 times compared to the defect-free bulk counterpart, while presents 6 times improvement compared to that of defect-free nanosheets.

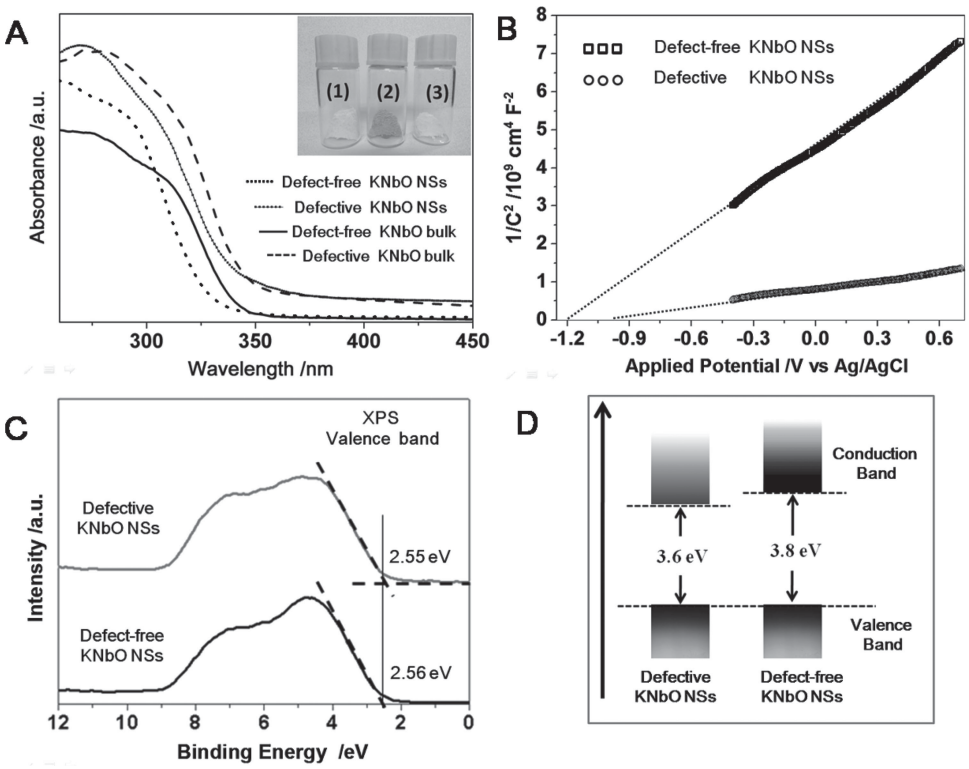

Figure 4. A) UV-visible absorption spectra of the defect-free $K_4Nb_6O_{17}$ nanosheets, defective $K_4Nb_6O_{17}$ nanosheets, defect-free $K_4Nb_6O_{17}$ bulk and defective $K_4Nb_6O_{17}$ bulk. Insert is the digital pictures of the defect-free $K_4Nb_6O_{17}$ nanosheets (1), defective $K_4Nb_6O_{17}$ nanosheets (2) and defective $K_4Nb_6O_{17}$ nanosheets after annealing (3). B) Mott–Schottky plots of the defect-free $K_4Nb_6O_{17}$ nanosheets and defective $K_4Nb_6O_{17}$ nanosheets. C) Valence band comparison of the defect-free $K_4Nb_6O_{17}$ nanosheets and defective $K_4Nb_6O_{17}$ nanosheets. D) Schematic illustration of the energy diagram for the defect-free $K_4Nb_6O_{17}$ nanosheets and the defective $K_4Nb_6O_{17}$ nanosheets.

Experimental Section

Preparation of $K_4Nb_6O_{17}$ bulk: $K_4Nb_6O_{17}$ bulk was prepared according to a literature method.[13] The stoichiometric amounts of K_2CO_3 and Nb_2O_5 were calcinated a in alumina crucible at 1100 K for 48 h.

Preparation of Ultrathin $K_4Nb_6O_{17}$ Nanosheets: Defect-free $K_4Nb_6O_{17}$ nanosheets were prepared via directly exfoliating the highly swelled $K_4Nb_6O_{17}{\cdot}3H_2O$ sheets in H_2O. The highly swelled $K_4Nb_6O_{17}{\cdot}3H_2O$ sheets were prepared as follows: 0.8 g Nb_2O_5 was added into 30 mL 1 M KOH solution. After vigorous stirring for 30 min, the mixture was transferred into a 45 mL Teflon-lined autoclave, sealed and heated at 220 °C for 24 h. The system was then allowed to cool down to room temperature naturally. The final product was first washed with distilled water. When the pH was close to neutralization, absolute ethanol was used to wash the product for several times, and then the precipitate was dried in vacuum at 60 °C overnight. In a typical exfoliation procedure, 10 mg flesh $K_4Nb_6O_{17}{\cdot}3H_2O$ sheets were added into 200 mL H_2O, then the suspension was ultrasonicated for 3 h. The resultant suspension was centrifuged at 4000 rpm for 5 minutes. After centrifugation, the supernatant was collected by pipette, and the typical yield is close to 100%. The final product was dried in vacuum at 60°C overnight for further characterization.

Preparation of Defective $K_4Nb_6O_{17}$ Nanosheets and Bulk: In a typical procedure, 100 mg ultrathin $K_4Nb_6O_{17}$ nanosheets were filled into a 2 ml quartz cuvette. Then the 2 ml quartz cuvette was put into a 6ml quartz cuvette with 200 mg KBH_4 added in advance. In order to promote the decomposition reaction of KBH_4, a 1 ml quartz cuvette filled with 100 μL H_2O was also put into the 6ml quartz cuvette. Finally, the 6ml quartz cuvette was sealed in a high-pressure autoclave and heated to different temperature at a rate of 5 °C/min, and maintained at this temperature for 12 h. The autoclave was then allowed to cool down to room temperature naturally. The defective $K_4Nb_6O_{17}$ bulk with an equivalent oxygen vacancy concentration was obtained via reducing the $K_4Nb_6O_{17}$ bulk in a similar procedure except changing the annealing time.

Characterization Methods: The samples were characterized by X-ray powder diffraction (XRD) by a Philips X'Pert Pro Super diffractometer equipped with graphite-monochromatized Cu-Kα radiation (λ = 1.54178 Å). The field emission scanning electron microscopy (FE-SEM) images were performed on a FEI Sirion-200. Tapping-mode atomic force microscopy (AFM) images were obtained on DI Innova Multimode SPM platform. Transmission electron microscopy (TEM) images were taken on H-7650 (Hitachi, Japan) operated at an acceleration voltage of 100 kV. High-resolution transmission electron microscope (HRTEM) images were operated on JEOL-2010 at an acceleration voltage of 200 kV. UV-Vis-NIR absorption spectra were recorded on a Perkin Elmer Lambda 950 UV-Vis-NIR spectrophotometer. X-ray photoelectron spectroscopy (XPS) measurements were performed on a VG ESCALAB MK II X-ray photoelectron spectrometer with an exciting source of Mg Kα = 1253.6 eV. Mott-Schottky plots were measured at a frequency of 10 Hz in the dark under the applied potentials from –0.8V to +0.5 V. EPR

NANO MICRO small

measurements were performed using a Bruker EMX plus model spectrometer operating at X-band frequencies (9.4 GHz) at 10K.

Photocatalytic Hydrogen Evolution Measurements: Photocatalytic hydrogen evolution reactions were carried out in a gas-closed circulation with vacuum. Typically, 10 mg photocatalyst powder was dispersed in 200 ml 20 Vol% CH_3OH aqueous solution via ultrasonication. The light source was a Xe lamp (300 W). The amount of hydrogen evolution was determined using a gas chromatograph (Agilent 7890A).

Supporting Information

Supporting Information is available from the Wiley Online Library or from the author.

Acknowledgements

This work was financially supported by the National Natural Science Foundation of China (11079004, 11321503, 21331005, 11175171), and the Chinese Academy of Sciences (XDB01020300).

[1] K. Maeda, K. Teramura, D. L. Lu, T. Takata, N. Saito, Y. Inoue, K. Domen, *Nature* **2006**, *440*, 295.
[2] X. B. Chen, S. H. Shen, L. J. Guo, S. S. Mao, *Chem. Rev.* **2010**, *110*, 6503.
[3] H. Tong, S. Ouyang, Y. Bi, N. Umezawa, M. Oshikiri, J. Ye, *Adv. Mater.* **2013**, *25*, 229.
[4] Y. Tachibana, L. Vayssieres, J. R. Durrant, *Nat Photonics* **2012**, *6*, 511.
[5] A. Kudo, Y. Miseki, *Chem. Soc. Rev.* **2009**, *38*, 253.
[6] a) Y. Wang, X. Wang, M. Antonietti, *Angew. Chem.* **2012**, *124*, 70; b) *Angew. Chem. Int. Ed.* **2012**, *51*, 68.
[7] G. Xie, K. Zhang, B. Guo, Q. Liu, L. Fang, J. R. Gong, *Adv. Mater.* **2013**, *25*, 3820.
[8] J. R. Swierk, T. E. Mallouk, *Chem. Soc. Rev.* **2013**, *42*, 2357.
[9] A. V. Akimov, A. J. Neukirch, O. V. Prezhdo, *Chem. Rev.* **2013**, *113*, 4496.
[10] S. Yang, Y. Gong, J. Zhang, L. Zhan, L. Ma, Z. Fang, R. Vajtai, X. Wang, P. M. Ajayan, *Adv. Mater.* **2013**, *25*, 2452.
[11] X. D. Zhang, Y. Xie, *Chem. Soc. Rev.* **2013**, *42*, 8187.
[12] H. X. Wang, Q. Wang, K. G. Zhou, H. L. Zhang, *Small* **2013**, *9*, 1266.
[13] M. C. Sarahan, E. C. Carroll, M. Allen, D. S. Larsen, N. D. Browning, F. E. Osterloh, *J. Solid. State. Chem.* **2008**, *181*, 1678.
[14] M. L. Guan, C. Xiao, J. Zhang, S. J. Fan, R. An, Q. M. Cheng, J. F. Xie, M. Zhou, B. J. Ye, Y. Xie, *J. Am. Chem. Soc.* **2013**, *135*, 10411.
[15] V. M. Zainullina, V. P. Zhukov, V. G. Zubkov, A. P. Tyutyunnik, *J. Struct. Chem.* **1998**, *39*, 627.
[16] X. Chen, L. Liu, P. Y. Yu, S. S. Mao, *Science* **2011**, *331*, 746.
[17] J. M. Rondinelli, N. A. Spaldin, *Adv. Mater.* **2011**, *23*, 3363.
[18] Y.-C. Lee, Y.-L. Chueh, C.-H. Hsieh, M.-T. Chang, L.-J. Chou, Z. L. Wang, Y.-W. Lan, C.-D. Chen, H. Kurata, S. Isoda, *Small* **2007**, *3*, 1356.
[19] a) Y. Ling, G. Wang, J. Reddy, C. Wang, J. Z. Zhang, Y. Li, *Angew. Chem.* **2012**, *124*, 4150; b) *Angew. Chem. Int. Ed.* **2012**, *51*, 4074.
[20] D. V. Bavykin, J. M. Friedrich, F. C. Walsh, *Adv. Mater.* **2006**, *18*, 2807.
[21] F. Zuo, L. Wang, T. Wu, Z. Zhang, D. Borchardt, P. Feng, *J. Am. Chem. Soc.* **2010**, *132*, 11856.
[22] M. Kong, Y. Li, X. Chen, T. Tian, P. Fang, F. Zheng, X. Zhao, *J. Am. Chem. Soc.* **2011**, *133*, 16414.
[23] I. Nakamura, N. Negishi, S. Kutsuna, T. Ihara, S. Sugihara, E. Takeuchi, *J. Mol. Catal. A* **2000**, *161*, 205.
[24] J. Gan, X. Lu, J. Wu, S. Xie, T. Zhai, M. Yu, Z. Zhang, Y. Mao, S. C. I. Wang, Y. Shen, Y. Tong, *Sci. Rep.* **2013**, *3*, 1021.
[25] R. Schaub, P. Thostrup, N. Lopez, E. Lægsgaard, I. Stensgaard, J. K. Nørskov, F. Besenbacher, *Phys. Rev. Lett.* **2001**, *87*, 266104.
[26] L. Liu, X. Zhao, H. G. Sun, C. Y. Jia, W. L. Fan, *ACS Appl. Mater. Interfaces.* **2013**, *5*, 6893.

Received: November 15, 2013
Revised: February 25, 2014
Published online: March 13, 2014

